Tracing life through light: towards detecting life on exoplanets with spectroscopy and spectropolarimetry

Mulder, W.

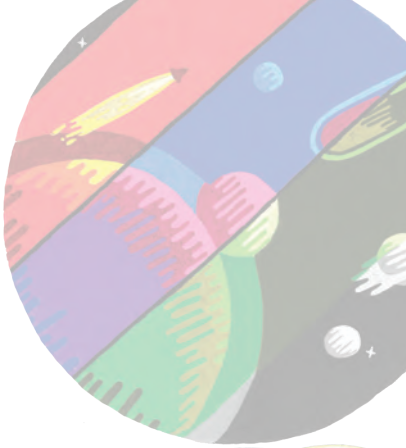

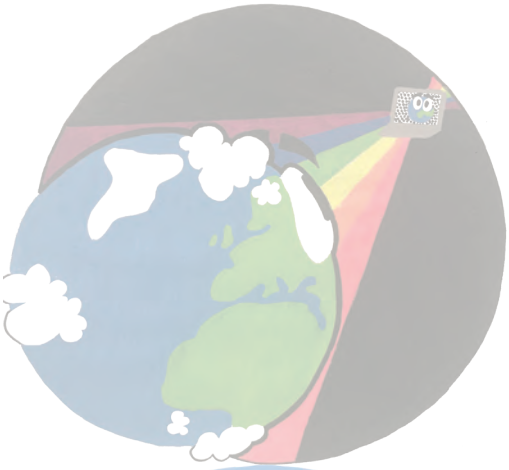

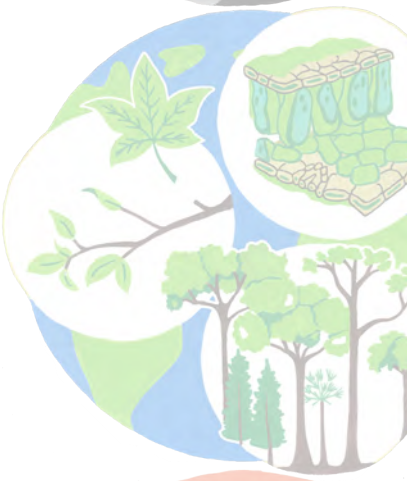


ANGRY PHOTONS


THE BEETLES

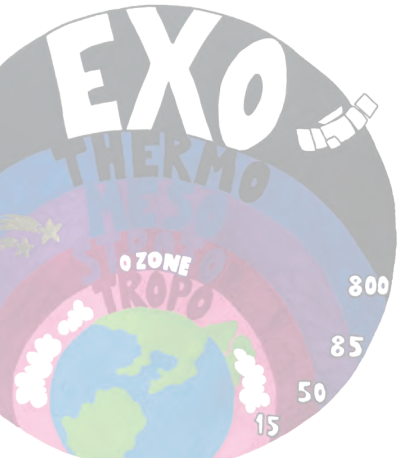
EXO
THERMO
OZONE
TROPO
800
85
50
15

1 | Introduction

With planetary exploration, there has been one general theme, and that is diversity. Everything is more diverse when we look at it than was predicted.

– Jack Lissauer, 2022

The revolutionary hunt for exoplanets and characterising atmospheres

How did we come into existence? Are we alone? These questions have driven humans for centuries. Despite long-standing speculations about extrasolar planets and extraterrestrial life, it was only three decades ago that astronomers discovered the first worlds beyond our solar system. In 1992, (Wolszczan & Frail, 1992) discovered planetary-mass objects orbiting the pulsar PSR B1257+12, believed to be second-generation products (Patruno & Kama, 2017) of stellar evolution. The first exoplanet around a main-sequence star was found by (Mayor & Queloz, 1995), marking the start of an exoplanet revolution and earning a Nobel Prize in 2019. This gaseous planet, 51 Pegasi b, orbits very close to its star, leading to the discovery of many "Hot Jupiters".

1.1 Exoplanet detection methods

Today, more than five thousand confirmed exoplanets have been discovered through methods like radial velocity, transit observations, and direct imaging. Figure 1.1 shows the wide diversity of the discovered exoplanets in terms of their mass and orbital period. It reveals classes that have no counterparts in the solar system, such as super-Earths and Hot Jupiters. Each of the before-mentioned detection methods are prone to detection biases and thus detection of specific types of exoplanets, as briefly explained below.

1.1.1 Radial-velocity method

A star with an orbiting planet experiences a gravitational pull from the planet, causing the star to wobble in a small orbit around the common centre of mass. The radial-velocity method, also known as Doppler spectroscopy, detects these wobbles as the Doppler shift of stellar spectral lines due to the periodic changes of the stellar velocity along the line of sight. The radial-velocity method provides only constraints on planetary masses, since the amplitude of the variation depends on the planet's mass, orbital distance and inclination. It is most sensitive to massive planets on close-in orbits, e.g. the first exoplanet discovery 51 Pegasi b, see Fig. 1.1, because signals with large amplitudes are easier to detect.

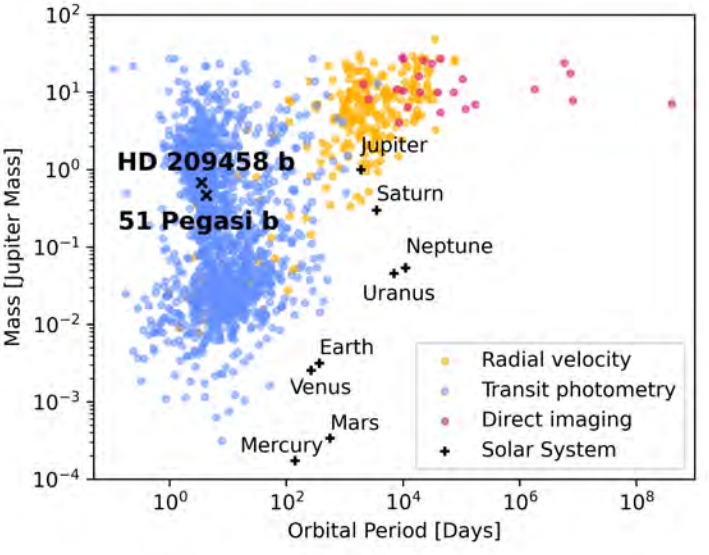

Figure 1.1: Mass of exoplanets plotted against their orbital period. The overview reveals the diverse population of all confirmed exoplanets to date (November, 24, 2025). The Solar System planets are marked using black crosses. The data, used in this figure, is coming from the NASA Exoplanet Archive.

However, stellar activity (e.g. rotation, spots and plages [1]) also induces apparent radial velocity variations, and these activity-driven signals can mimic or obscure the Doppler wobble of a planet. This makes the identification of low-amplitude planetary signals particularly challenging when the planet's orbital period is similar to the characteristic timescales of stellar activity. Over the years, the precision of radial velocity measurements has improved significantly as highly sensitive spectrographs are able to detect rocky planets around low-mass stars, and the stellar velocity signal becomes smaller as the planets are more distant, e.g. Proxima Centauri b and d (e.g. Anglada-Escudé et al., 2016; Faria et al., 2022) and planets with even longer orbital periods (e.g. Dubber et al., 2019).

1.1.2 Transit photometry

After the discovery of the first five planets around solar-type stars, photometric searches had been carried out to try to detect planet transits, however without success (e.g. Henry et al., 1997; Baliunas et al., 1997; Henry et al., 2000). These early surveys lacked the continuous, high-precision photometry required to detect the shallow and infrequent dips caused by most planets. It was not until 1999, when Charbonneau et al. (1999) was the first to use the transit method to find the hot Jupiter orbiting the G0 dwarf HD 209458, the first exoplanet for

[1] Plages are bright, elongated regions on a star's surface, often associated with star spots and strong magnetic fields, that are a key part of stellar activity. star spots, however, appear as dark spots.

which a transit was observed after its initial radial-velocity discovery. The planet received the designation HD 209458 b, see Fig. 1.1.

The exoplanet discoveries with the space missions CoRoT (Baglin et al., 2009), Kepler (Howell et al., 2014) and TESS (Ricker et al., 2015) completely changed the field of exoplanets, as these missions enabled continuous, ultra-precise photometric monitoring of large stellar samples and revealed thousands of small planets. Ever since the data release of Kepler in 2014, transit photometry has been the most widely used technique for detecting and studying exoplanets. The mission carried out accurate photometry of many stars and searched for dips in their light curves caused by orbiting exoplanets that block parts of the starlight. This already implies that the orbits need to be aligned near edge-on from our viewpoint, and that only a small geometric fraction of planetary systems can be detected in transit.

The depth of the dips in the transit light curves are used to determine the radii of the planets, whereas observing multiple transits allows for the determination of the orbital period. Therefore, just as for the radial-velocity method, transit photometry is most effective for detecting larger exoplanets with shorter orbital periods, because these produce deeper and more frequent transit signals and are easier to distinguish from noise.

Combining the latter methods breaks the degeneracy of the planet mass and orbital inclination and therefore provides a method to determine the bulk density given the planet mass and radius, yielding a direct constraint on the planet's internal structure and composition.

1.1.3 Direct imaging

The direct depiction of an exoplanet on an image requires a method to angularly resolve the dim planet from its host star. To do so, an imaging system needs to overcome the huge contrast between the star and the planet at small angular separations. This requires so-called High Contrast Imaging (HCI). For example, in the optical wavelength regime, the detection of light reflected off an Earth-like planet orbiting a Sun-like star, requires a contrast of $\sim 10^{-10}$ and for a Jupiter-analogue a contrast of $\sim 10^{-8} - 10^{-9}$ relative to their host star. In the near-infrared regime, young giant planets generally have contrasts in the range $10^{-4} - 10^{-6}$. The majority of the heat from their formation is emitted as near-infrared radiation. It remains the region of most favourable contrast even as planets age, improving the $\sim 10^{-8} - 10^{-9}$ contrast ratio to $\sim 10^{-5}$ for the same Jupiter-analogue. Current ground-based high-contrast imaging instruments can directly image bright self-luminous brown dwarf companions in NIR total intensity at contrasts of $10^{-2} - 10^{-6}$ (e.g. Nielsen et al., 2019; Langlois et al., 2021).

Achieving high contrasts at small angular separation requires adaptive optics (compensating atmospheric disturbances of the incoming light using wavefront sensing and a deformable mirror and allowing diffraction-limited imaging), coronagraphy (blocking on-axis starlight and with that boosting the contrast of the off-axis companions, (e.g. Lyot, 1939; Ferrari et al., 2007), and advanced data processing techniques for optimal suppression of the remaining starlight like e.g. Spectral Differential Imaging (SDI; Racine et al., 1999), Polarimetric Differential Imaging (PDI; Kuhn et al., 2001), Imaging Spectroscopy (IS; Sparks & Ford, 2002) or Angular Differential Imaging (ADI; Marois et al., 2006).

In 2004, Chauvin et al. (2004) was the first to directly image an exoplanet using the Very Large Telescope (VLT). It concerned the planetary mass object 2M1207 b orbiting a brown

dwarf. This so-called 'Super Jupiter' has a mass of a bit more than five Jupiter masses. To date, 82 planets have been directly imaged, including about 50 other Super Jupiters. These gas giants function as a laboratory for understanding the atmospheric physics of substellar objects and their possible link to planet formation.

Investigating the diversity of exoplanets with direct imaging

There are two main planet formation theories that could explain the resulting diverse planetary systems: the core-accretion (Pollack et al., 1996) and the disk gravitational instability (Boss, 1997) models. In the core-accretion model, dust grains in a protoplanetary disk gradually collide and grow into massive solid cores (a few Earth masses), which then trigger rapid gas accretion to form giant planets over millions of years. In contrast, the disk gravitational instability model envisions that in a massive, cool disk, parts of the gas rapidly collapse under their own gravity - on dynamical timescales of thousands of years - forming self-gravitating clumps that can contract into gas giants, especially in the disk's outer regions. The former explains the observed metallicity correlation and prevalence of gas giants at moderate orbital distances, while the latter provides a fast route to giant planet formation in massive or at larger orbital distances. Circumstellar disks are used to investigate these formation processes as they shape the planet-forming environments (e.g. Mizuno, 1980; Harsono et al., 2018; Keppler et al., 2018). Focusing on polarimetric observations, in the last few decades PDI has been used to image bipolar and cometary nebulae (Gledhill, 1991) and protoplanetary nebulae (Gledhill et al., 2001). Recently van Holstein et al. (2021) reported the polarimetric detections of the substellar companions DH Tau B and GSC 6214-210 B, likely originating from the circumsubstellar accretion disk. PDI records two orthogonal linear polarisation states simultaneously on the detector (Andreou & Kalayjian, 2002; Dohlen et al., 2008; de Boer et al., 2020). The emission from an unresolved host star is predominantly unpolarised (Kemp et al., 1987) and results in two nearly identical beams, whereas the stellar light that has been reflected on dust grains becomes polarised through scattering. As a result, the starlight will be largely removed during the post-processing and the reflected polarised light will reveal itself. These scattered-light observations do not only reveal the presence of dust particles, but also provide information regarding the properties of dust grains, as encoded in the intensity and degree of polarisation as a function of phase angles and wavelength (Ginski et al., 2023). This provides us with valuable insights into the birth environment of planets.

1.2 From detecting to characterizing exoplanets

An initial understanding of the bulk density of the discovered exoplanets can be achieved by combining the transit and radial velocity techniques. Nevertheless, significant ambiguities complicate the in-depth analysis of exoplanet compositions when relying solely on mass and radius measurements (Seager et al., 2007). Additional spectroscopic observations of exoplanet atmospheres yield details concerning their thermal structures, dynamic behaviours and atmospheric composition with possible leftover molecules from their birthplaces (e.g. Madhusudhan et al., 2014; Thiabaud et al., 2014), clarifying their formation history.

1.2.1 Transmission spectroscopy

In the case of a planet transiting its host star, some starlight is blocked by the planet while some shines through the upper layers of the planet's atmosphere. The light is absorbed and scattered by aerosols and molecules, leading to a wavelength-dependent absorption in the stellar spectrum. Consequently, measuring the transit depth as a function of wavelength allows for the identification of chemical species in the exoplanet's atmosphere (Seager & Sasselov, 2000).

The first detection of a chemical species in an exoplanetary atmosphere was the identification of the sodium doublet in HD 209458 b. Charbonneau et al. (2002) found a slight enhancement of the transit depth of the planet at the sodium-line wavelengths. Thereafter, other species like water (e.g. Deming et al., 2013; Evans et al., 2016) and more recently molecules including CO_2 (e.g. Ahrer et al., 2022; Madhusudhan et al., 2023; Rustamkulov et al., 2023), SO_2 (Tsai et al., 2023), CH_4 (Bell et al., 2023; Madhusudhan et al., 2023) and H_2S (Fu et al., 2024) using JWST.

1.2.2 Emission spectroscopy

During a secondary eclipse, the thermal radiation and reflected light from a planet will disappear and reappear. The (near-)infrared radiation emitted by the exoplanet is observed by comparing the flux of the planetary system before, after, and during its secondary eclipse (e.g. Richardson et al., 2003; Charbonneau et al., 2005). This observational method, referred to as emission spectroscopy, enables the characterization of the planetary atmosphere properties such as the pressure-temperature profile (P-T profile), molecular composition, and cloud properties (Madhusudhan, 2019). Additionally, it can probe the temperature structure on the daysides of these planets (e.g. Cubillos et al., 2011; Yan, F. et al., 2022), and infer the presence of potential thermal inversions (e.g. Burrows et al., 2007; Knutson et al., 2008).

1.2.3 High-resolution Doppler spectroscopy

High-resolution Doppler spectroscopy plays a crucial role in our understanding of exoplanet atmospheres, offering insights into the chemical composition, dynamics, and physical conditions of exoplanets. Similar to the radial-velocity method, Doppler spectroscopy relies on the Doppler shift of spectral lines. In addition, it takes advantage of the relative large radial velocity of the companion compared to its host star.

The high spectral resolution disperses into a larger number of spectral channels, which significantly decreases the signal-to-noise per channel. One way to compensate for this loss is using the cross-correlation technique. It measures the similarity of a spectrum reflecting one or more species or even a full atmospheric model shifted with various radial velocities and the observational data. In addition, the high resolution ensures that the spectral features of different species can be resolved into unique ensembles of individual lines, allowing the unambiguous identification of even minor species and isotopologues (Mollière & Snellen, 2019; de Regt et al., 2024; González Picos et al., 2024; Gandhi et al., 2025).

Snellen et al. (2010) was the first to successfully apply high-resolution spectroscopy on the transiting hot Jupiter HD 209458 b using the CRyogenic high-resolution InfraRed Echelle

Spectrograph (CRIRES; Kaeufl et al., 2004) instrument on the VLT. CRIRES was designed for high-resolution spectroscopy in the infrared. This is particularly useful for detecting molecules in the atmospheres of cooler exoplanets, which emit more strongly in the infrared part of the spectrum. The instrument was recently upgraded to CRIRES+ (Dorn et al., 2023) with cross-dispersing elements and larger, more sensitive detectors. The simultaneous wavelength range increased by a factor of ~ 10, while preserving the total operational wavelength range.

1.2.4 Atmospheric models & retrievals

High-resolution spectroscopy allows us to quantify the species and isotopologues in the atmospheres of extrasolar objects. To do so, we apply an atmospheric retrieval technique that couples an atmospheric model of the object's atmosphere with a nested sampling tool to obtain the posterior distributions of the given parameters of the object. Our models make use of a 'free chemistry' temperature profile. It allows the chemical abundances to vary freely within fixed boundaries, while being vertically constant throughout the atmosphere. This 'free' retrieval offers a high degree of flexibility. The parameter space is initiated by a set of priors and boundary constraints for a set of parameters describing the atmospheric chemistry, cloud structure, surface gravity, and molecular or atomic opacities. This technique has been applied to various exoplanets (e.g. Crossfield et al., 2019; Welbanks et al., 2019; Mollière et al., 2020; Zhang et al., 2022; Grasser et al., 2024; Landman et al., 2024; Xuan et al., 2024), and other self-luminous objects, like brown dwarfs (e.g. González Picos et al., 2024; de Regt et al., 2024; Gandhi et al., 2025; Mulder et al., 2025).

The atmospheric retrieval framework used in this chapter is based on the radiative transfer code `petitRadTrans` (`pRT`; Mollière et al., 2019). It is a powerful Python interface to calculate planetary transmission and/or emission spectra (including multiple scattering). `pRT`'s built-in retrieval package provides the option to run retrievals that combine data sets of varying resolution, wavelength coverage and atmospheric contexts. `pRT`'s extensive opacity database includes gas and cloud opacities. `pRT` was integrated with the nested sampling tool `PyMultiNest` (Buchner et al., 2014), a Python interface for the `MultiNest` algorithm.

A significant and time expensive number of `pRT` model spectra are needed to statistically support the retrievals. To speed up the process, the spectral computations were sped up by undersampling the high-resolution spectra, i.e. by a factor of 3). All computations were executed in parallel on the Dutch National Supercomputer Snellius.

1.3 Current and future research in exoplanetary science

1.3.1 Observational probes of planet formation history

Isotopes in exoplanet atmospheres have the potential to provide important insights into the origin and evolution of planetary systems. In the Solar System, the deuterium-to-hydrogen (D/H) ratio traces the origin and evolution of water within our own celestial neighbourhood. Therefore, it can function as a key diagnostic to determine where objects were formed. Also outside the Solar System, the D/H ratio may vary for different exoplanets. This variation

may be linked to the varying isotope ratios in the protoplanetary disks that are caused by deuterium fractionation due to temperature differences (Aikawa & Herbst, 1999; Ceccarelli et al., 2014). Deuterium fractionation arises because the heavier deuterium-bearing molecules have slightly lower zero-point energies than their protium (^{1}H) counterparts, making ion–molecule exchange reactions (e.g., $H_3^+ + HD \rightarrow H_3D^+ + H_2$) strongly favoured at low temperatures. As a result, cold regions of protoplanetary disks become enriched in deuterium relative to hydrogen, while warmer areas support less fractionation and can even reverse it through exchange with HD and H_2O, producing the spatial D/H variations observed in exoplanet-forming material. The D/H ratio may change over time after a planet is formed, as atmospheric loss processes can still alter the D/H ratio.

Carbon and oxygen are two of the most abundant elements in the universe and play key roles in the chemistry of protoplanetary disks and planetary atmospheres. A disk midplane, the region where planets form, a radial gradient in the gas–ice C/O ratio is expected due to temperature-dependent freeze-out of major volatiles (Öberg et al., 2011). As molecules such as H_2O, CO_2 and CO condense at progressively larger orbital distances, this creates chemically distinct zones in which either carbon- or oxygen-rich material dominates the gas or solid phase. Planets assembling in these regions may therefore inherit characteristic atmospheric C/O ratios.

However, recent studies suggest that this simple static picture is likely incomplete. The radial transport of solids - particularly the inward drift of icy pebbles - can redistribute volatile ices across large distances, altering both the local gas-phase and solid-phase C/O ratios (e.g. Schneider & Bitsch, 2021; Eistrup & Henning, 2022). The sublimation of drifting pebbles inside their respective ice lines can locally enrich the gas with oxygen- or carbon-bearing species, smoothing or even reversing the expected radial gradients. As a result, the C/O ratio imprinted on forming planets may be influenced not only by the nominal ice-line locations, but also by the efficiency of pebble drift, the disk's dust-to-gas ratio, and the evolutionary stage of the disk.

Some isotope ratios are (roughly) constant on Solar System scales. (Woods & Willacy, 2009) measured a carbon $^{12}C/^{13}C$ isotope ratio of ~89. On larger, galactic scales, the ratio varies. ^{13}C is produced within stars that enrich the interstellar medium over time. The current, local ISM has an average $^{12}C/^{13}C$ ratio of ~68 (Langer & Penzias, 1993; Milam et al., 2005), which is significantly lower than that of the Solar System. Similar to deuterium fractionation, fractionation processes could create isotope-ratio variations on protoplanetary disk scales (Woods & Willacy, 2009), which could be passed on to exoplanet atmospheres (Zhang et al., 2021; Mollière et al., 2019; Line et al., 2021; Bergin et al., 2024).

High-resolution spectroscopy has proven to be able to constrain isotopic compositions of BDs, as Zhang et al. (2021) illustrated using the NIRSPEC instrument on the Keck telescope and de Regt et al. (2024) using CRIRES+ on the VLT. This opens up the possibility of investigating the carbon $^{12}C/^{13}C$ isotope ratio as a formation tracer. Additional isotope ratios might be within the reach of current high-resolution spectrographs, such as CRIRES+, and space-based facilities, such as JWST (Gandhi et al., 2023). Looking further ahead, the ex-

tremely large telescope will include a high-resolution spectrograph operating in the infrared regime (METIS; Brandl et al., 2021) and the Giant Magellan Telescope (GMT) one operating in the optical regime (GCLEF; Szentgyorgyi et al., 2016). These new instruments will make substantial advances with high-resolution spectroscopy by detecting minor chemical species in both BDs and exoplanet atmospheres, e.g. possibly identifying biomarkers in rocky planet atmospheres.

1.3.2 Working towards the search for extraterrestrial life

The search for life in the universe is a driving force for (exo)planetary research. On average, every star hosts at least one planet (Cassan et al., 2012), and one in two Solar-like stars could host a rocky planet in their habitable zone (Hsu et al., 2019; Bryson et al., 2021).

The observation of a transit requires a planetary system with a specific edge-on geometry. As a result, many of the potential close-by Earth-like planets will be missed. In addition, in the case of an optimal orientation, there will be only one transit every year when considering Earth-like planets around Sun-like stars. Even if we would observe a transit, many observations would be required to obtain a high enough signal-to-noise ratio to detect biosignatures (Serindag & Snellen, 2019; Hardegree-Ullman et al., 2023).

In the end, direct imaging may offer the best means to detect possible life on other planets. There is still much work to be done before instruments can reach the required contrasts to detect Earth-like planets using reflected starlight. In the coming years, there will be a large focus on the development of (new) technology (e.g. adaptive optics focal-plane wavefront sensing techniques (Haffert et al., 2023), predictive control (e.g. Males & Guyon, 2018; Landman et al., 2021; Haffert et al., 2021), development of very high-order deformable mirrors), improving post-processing algorithms (e.g. SDI, PDI, IS and ADI), and the construction of large ground- and space-based observatories. The Nancy Grace Roman Space Telescope will be testing the first dedicated high-contrast imaging instrument in space (Kasdin et al., 2020). The main science goal of NASA's Habitable World Observatory will be to directly image Earth-like planets in the habitable zone of Sun-like stars, and identify biosignatures in their atmosphere. European Southern Observatory's Extremely Large Telescope will have instruments such as METIS (Brandl et al., 2021) that will push the capabilities of ground-based high-resolution spectroscopy to smaller planets and more detailed characterization of their atmospheres. Proxima Centauri b would be a prominent target, which may be detectable when combining high-contrast imaging with high-dispersion spectroscopy on the Extremely Large Telescope (Snellen et al., 2015). Adaptive optics will be the most crucial technology for ground-based high-contrast imaging, bringing detection of potential biomarker gases within reach within the next decade.

1

Who are we? We find that we live on an insignificant planet of a humdrum star lost in a galaxy tucked away in some forgotten corner of a universe in which there are far more galaxies than people.

– Carl Sagan, 1980s

Observing the Earth as an Exoplanet using spectropolarimetry

To detect extraterrestrial life, we need dedicated instruments, data-analysis algorithms and observation strategies; what are we looking for? New opportunities will emerge once the technology is ready to resolve Earth-like planets from their host stars. Direct-imaging spectroscopy and polarimetry will open up another source of information by studying the properties of planets via spectral flux and polarisation measurements. Light emitted by a solar type star is in general unpolarised when integrated over the stellar disk (Kemp et al., 1987). Light observed from a planet will usually be polarised, since starlight is scattered by particles and aerosols in its atmosphere, or reflected by a surface (in the case of a rocky planet). In theory, the atmosphere of an exoplanet could be characterized, without even optically resolving the planet since the polarisation depends on the physical circumstances of the scatterers, e.g. their shapes, sizes and chemical composition. Polarised radiative transfer simulations have shown that light reflected by an Earth-like exoplanet is indeed polarised by either surface reflection or atmospheric scattering (e.g. Hansen & Travis, 1974; Stam, 2008; Karalidi et al., 2012; Trees & Stam, 2019). The degree and the direction of polarisation also depend on the viewing geometries and wavelength (e.g. Groot et al., 2020; Gordon et al., 2023, and references therein). This allows us to use polarimetry to detect traces of bio-signatures and possibly extraterrestrial life.

Despite the strong astronomical science cases that polarimetry has to offer, polarimetry has not been featuring in any space telescope as a first science goal, yet. However, space missions have delivered valuable polarimetric insights by carrying instruments or filters capable of measuring polarisation. For example, the NICMOS instrument on the Hubble Space Telescope underwent a dedicated nine-orbit calibration during Cycle 15, enabling high-accuracy near-infrared imaging polarimetry (~1% precision) of circumstellar structures. In addition polarimetric observations of comet ISON at a distance of 3.8 astronomical unit, made with Hubble's ACS-WFC instrument, provided the first sub-arcsecond visible-light polarisation maps of an Oort-cloud comet, revealing distinct dust-jet signatures.

The Nancy Grace Roman Space Telescope will be the first space-based observatory demonstrating high-contrast polarimetry using the Roman Coronagraph (Doelman et al., 2023). Its implementation presents trade-offs for both imaging and spectroscopy. All components in an instrument may change or add to the incoming polarisation of the incident light, complicating the calibration and observation strategies. Furthermore, polarisation optics reducing the intensity of incoming light (even up to a half) are unfavourable in the field of exoplanetary science, where photons are scarce. Moreover, polarimetry, being a differential technique, usually comes with all kinds of systematic errors, like spurious polarisation signals created by varying atmospheric properties, imperfect (knowledge of the) optics or

even detector properties. To this end, the implementation of polarimetry in an astronomical instrument requires a careful instrument design.

1.4 Definitions for polarimetry

The study of polarisation requires precise definitions, as the interpretation of polarimetric measurements depends critically on the underlying concepts. Polarisation is a property of transverse waves which specifies the geometrical orientation of the electric field vector of light. The definition of polarisation is widely explained and discussed in literature (e.g. Collett, 2005; Goldstein, 2011; Hecht, 2017; Pedrotti et al., 2019).

Follow the definition according to Hecht (2017), we describe polarisation using the Jones and the Stokes formalism. The Jones formalism is limited to treating fully polarised electromagnetic beams and their phase information. The formulation is applicable to perfectly coherent beams, which does allow a description of interference phenomena, however, it can neither describe randomly (better known as unpolarised) or partially polarised light nor the depolarisation of light. In the intensity domain, a beam can be described with the Stokes formalism. This formalism can describe full, partially and unpolarised light. Phenomena like interference cannot be represented with the Stokes formalism, as it does not contain phase information.

1.4.1 Jones formalism

The Jones formalism is able to handle coherent waves, meaning that the phase information is preserved. Each electro-magnetic beam can be represented in terms of the electric field vector components. Therefore, in column form, the 2×1 (complex) Jones vector is:

$$\mathbf{E} = \begin{bmatrix} E_x \\ E_y \end{bmatrix} = \begin{bmatrix} E_{0x} e^{i\varphi_x} \\ E_{0y} e^{i\varphi_y} \end{bmatrix}, \tag{1.1}$$

where E_{0x} and E_{0y} are the amplitudes and φ_x and φ_y are the phases. Linear, circular, and elliptical polarisation correspond to special cases of the relative amplitudes and phase difference between E_x and E_y. Linear polarisation arises when the phase difference is zero or π, circular when the amplitudes are equal and the phase difference is $\pm\pi/2$, and elliptical in the general case. Two orthogonal linear polarisation states are represented by substituting either $E_{0y} = 0$ for fully horizontal, see Eq. 1.3, and $E_{0x} = 0$ for vertical polarisation:

$$\mathbf{E}_{\text{hor}} = \begin{bmatrix} E_{0x} e^{i\varphi_x} \\ 0 \end{bmatrix} \qquad \mathbf{E}_{\text{ver}} = \begin{bmatrix} 0 \\ E_{0y} e^{i\varphi_y} \end{bmatrix} \tag{1.2}$$

The sum of two coherent beams is simply the sum of their corresponding components. For simplicity, the irradiance can be normalized to unity when the exact amplitude and phase are not of importance, resulting in the vectors:

$$\vec{\mathbf{E}}_{\text{hor}} = \begin{bmatrix} 1 \\ 0 \end{bmatrix} \qquad \vec{\mathbf{E}}_{\text{ver}} = \begin{bmatrix} 0 \\ 1 \end{bmatrix} \tag{1.3}$$

After a polarised incident beam $\mathbf{E}_{\text{in}}$ passes through a series of n optical elements, $\mathbf{J}_1, \mathbf{J}_2, \cdots \mathbf{J}_n$, the outgoing modified Jones vector equals $\mathbf{E}_{\text{out}} = \mathbf{J}_n \cdots \mathbf{J}_2 \mathbf{J}_1 \mathbf{E}_{\text{in}}$. Each matrix $\mathbf{J}_i$ is a 2×2 Jones matrix, that represents the interaction with a single optical element;

$$\mathbf{J} = \begin{pmatrix} j_{xx} & j_{xy} \\ j_{yx} & j_{yy} \end{pmatrix}. \tag{1.4}$$

For an ideal linear polariser the off-diagonal elements $j_{yx} = j_{xy}$ are 0 and the diagonal elements have a value between 0 and 1, see Eq. 1.5. As a result, this element only changes the amplitude of the incoming Jones vector, while its phase remains the same.

$$\mathbf{J}_{\text{hor,pol}} = \begin{pmatrix} 1 & 0 \\ 0 & 0 \end{pmatrix}, \qquad \mathbf{J}_{\text{ret}} = e^{i\delta/2} \begin{pmatrix} 1 & 0 \\ 0 & -i \end{pmatrix}. \tag{1.5}$$

As the name reveals, a wave plate changes the phase φ_x and φ_y of the incoming wave with a given retardance δ. As a result, for a wave plate the off-diagonal elements are again zero, however, we add a phase shift of $\varphi_x = \delta/2$ along the x-axis, $j_{xx} = e^{i(\delta/2)}$ and $\varphi_y = -\delta/2$ along the y-axis, $j_{yy} = e^{-i(\delta/2)}$). The retardance equals $\delta = \pi$ for a half-wave plate and $\delta = \pi/2$ for a quarter-wave plate.

1.4.2 Stokes and Mueller formalism

Light is generally neither completely polarised nor completely unpolarised; more often, it is partially polarised, with the electric-field vector varying in a statistically incoherent manner, typically described in terms of photon fluxes. A useful way to characterise such light is as a superposition of specific proportions of unpolarised and polarised components. Stokes (1852) introduced four observables to describe any such superposition: the Stokes polarisation parameters `I`, `Q`, `U`, and `V`, which together form the so-called Stokes vector, $\mathbf{S}$ (Stokes, 1852; Chandrasekhar, 1946):

$$\mathbf{S} = \begin{pmatrix} S_0 \\ S_1 \\ S_2 \\ S_3 \end{pmatrix} = \begin{pmatrix} \langle E_x^* E_x + E_y^* E_y \rangle \\ \langle E_x^* E_x - E_y^* E_y \rangle \\ \langle E_x^* E_y + E_y^* E_x \rangle \\ \langle i\left(E_y^* E_x - E_x^* E_y\right) \rangle \end{pmatrix} = \begin{pmatrix} I_{0^\circ} + I_{90^\circ} \\ I_{0^\circ} - I_{90^\circ} \\ I_{45^\circ} - I_{-45^\circ} \\ I_{\circlearrowright} - I_{\circlearrowleft} \end{pmatrix} = \begin{pmatrix} \texttt{I} \\ \texttt{Q} \\ \texttt{U} \\ \texttt{V} \end{pmatrix} \tag{1.6}$$

The second definition in Eq. 1.6 shows the calculation of the Stokes vector as ensemble of the averages and covariances of the electric field vector components. The third definition provides a description on how to measure the Stokes parameters using flux measurements through linear polarisers at certain angles and either left- or right-handed circular polarisers.

In the literature, the Stokes parameters are represented as S_0, S_1, S_2, S_3, as well as `I`, `Q`, `U` and `V`. To prevent confusion, we will only use the latter. The first Stokes parameter, `I`, represents the total intensity of the optical beam; the second and third, `Q` and `U`, describe the linear polarisation state and are defined as differential intensity measurements between orthogonal linear bases. The fourth parameter, `V`, quantifies the circularly polarised component as the difference between right- and left-handed circular polarisation intensities. In this dissertation, we refer to the horizontal, vertical, 45° and 135° linear polarisation states

as Q+, Q−, U+, U−, whereas V+ and V− represent right- and left-handed circular polarisation. Throughout the text, when fractional polarisation is discussed, the absolute values of Q, U and V are normalized with respect to the intensity I.

Measurements of incoming polarisation from inclined or moving platforms - such as airborne remote sensing - are susceptible to small errors in the reference orientation used to define viewing angles. This poses a particular challenge for interpreting the linear Stokes parameters, Q and U, which depend explicitly on the choice of reference frame. In such cases, it is often more practical to derive orientation-independent quantities such as the degree of polarisation, P, which describes the fraction of the wave that is polarised, as well as the degree and angle of linear polarisation, P_{L} and χ_{L} respectively.

$$P = \frac{\sqrt{\mathtt{Q}^2 + \mathtt{U}^2 + \mathtt{V}^2}}{\mathtt{I}}; \qquad P_{\mathrm{L}} = \frac{\sqrt{\mathtt{Q}^2 + \mathtt{U}^2}}{l}; \qquad \chi_{\mathrm{L}} = \frac{1}{2}\arctan\frac{\mathtt{U}}{\mathtt{Q}}. \tag{1.7}$$

These quantities remain well-defined regardless of the exact reference orientation, making them more robust for field applications.

Mueller calculus

Stokes vectors can be manipulated using the Mueller calculus. A single or a stack of multiple optical elements can be represented by a 4×4 Mueller Matrix, $\mathbf{M}$. If an incoming beam of light with a given polarisation state, $\mathbf{S}_{\mathrm{in}}$, propagates through an element $\mathbf{M}$, the observed outgoing beam $\mathbf{S}_{\mathrm{obs}}$ is linearly related to $\mathbf{S}_{\mathrm{in}}$, through $\mathbf{S}_{\mathrm{obs}} = \mathbf{M}\mathbf{S}_{\mathrm{in}}$. This can be expressed in terms of Mueller matrix elements $m_{\mathrm{i,j}}$ as:

$$\begin{pmatrix} \mathtt{I}_{\mathrm{obs}} \\ \mathtt{Q}_{\mathrm{obs}} \\ \mathtt{U}_{\mathrm{obs}} \\ \mathtt{V}_{\mathrm{obs}} \end{pmatrix} = \begin{pmatrix} m_{11} & m_{12} & m_{13} & m_{14} \\ m_{21} & m_{22} & m_{23} & m_{24} \\ m_{31} & m_{32} & m_{33} & m_{34} \\ m_{41} & m_{42} & m_{43} & m_{44} \end{pmatrix} \begin{pmatrix} \mathtt{I}_{\mathrm{in}} \\ \mathtt{Q}_{\mathrm{in}} \\ \mathtt{U}_{\mathrm{in}} \\ \mathtt{V}_{\mathrm{in}} \end{pmatrix} \tag{1.8}$$

Mueller matrices can describe optics that (de)polarise and/or change the phase of the light. For example, the Mueller matrix for a perfect, horizontal polariser and a retarder with retardance δ with the fast axis orientation in the +Q direction are given by

$$\mathbf{M}_{\mathrm{hor,pol}} = \frac{1}{2}\begin{pmatrix} 1 & 1 & 0 & 0 \\ 1 & 1 & 0 & 0 \\ 0 & 0 & 0 & 0 \\ 0 & 0 & 0 & 0 \end{pmatrix}, \qquad \mathbf{M}_{\mathrm{ret}} = \begin{pmatrix} 1 & 1 & 0 & 0 \\ 1 & 1 & 0 & 0 \\ 0 & 0 & \cos\delta & \sin\delta \\ 0 & 0 & -\sin\delta & \cos\delta \end{pmatrix}. \tag{1.9}$$

If an optical component is rotated with an angle θ, its Mueller matrix is multiplied with a rotation matrix, $\mathbf{M}(\theta) = \mathbf{M}_{\mathrm{rot}}(-\theta) \cdot \mathbf{M} \cdot \mathbf{M}_{\mathrm{rot}}(\theta)$, where the rotation matrix is given by

$$\mathbf{M}_{\mathrm{rot}}(\theta) = \begin{pmatrix} 1 & 0 & 0 & 0 \\ 0 & \cos 2\theta & \sin 2\theta & 0 \\ 0 & -\sin 2\theta & \cos 2\theta & 0 \\ 0 & 0 & 0 & 1 \end{pmatrix} \tag{1.10}$$

1.4.3 Scattering and phase matrix

The Jones and Stokes formalisms generally assume that the propagation direction of a beam of light remains unchanged. In applications where the direction is constant - such as through uniform optical elements - they provide powerful tools for analysing polarisation changes without the need for complex directional scattering considerations. For scenarios involving reflection or refraction, such as the Fresnel effect, the associated Mueller matrix implicitly accounts for changes in direction and amplitude due to the interface. *Scattering and phase matrices* do include the change in propagation direction after a scattering event. Scattering matrices account for changes in the propagation direction that occur when light interacts with particles (e.g., in a planetary atmosphere or with biotic molecules on a planetary surface). The phase matrix captures both the angular distribution of scattered light and changes to the polarisation state due to scattering. It describes how an incident wave transforms into a scattered wave in terms of both its direction and polarisation.

Chandrasekhar (1950) and Hovenier (1971) advanced the theory of radiative transfer, allowing for a quantitative description of scattered light in terms of Stokes parameters. By linking these parameters to phase and scattering matrices, researchers can rigorously describe how intensity and polarisation evolve through complex media, providing insights into the optical properties of particles and surfaces in various environments.

Scattering geometries

The direction of scattering after a scattering event is given by the scattering angle, $0 \leq \Theta \leq \pi$, and the azimuth angle, $0 \leq \varphi \leq 2\pi$, see Fig. 1.2. Θ is the cosine of the angle between the direction of the incident (ϑ, φ) and scattered $(\vartheta\prime, \varphi\prime)$ beam. ϕ the azimuth angle measured in the clockwise direction.

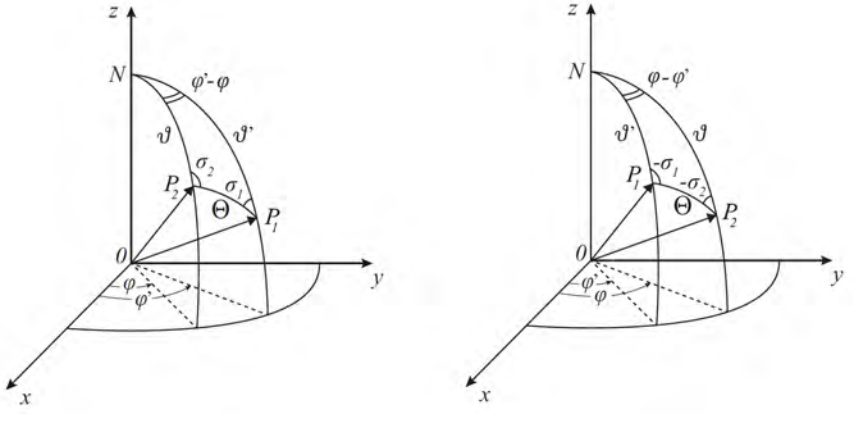

Figure 1.2: The geometry of scattering event at O, where OP_1 and OP_2 are the directions of the incident and scattered light. The azimuth difference is $0 < \phi' - \phi < \pi$ and $0 < \phi - \phi' < \pi$ for the **left** and **right panel**, respectively. Image credits Hovenier & van der Mee (1983).

Scattering matrix

The *scattering matrix*, $\mathbf{F}(\Theta)$, transforms the Stokes vector of the incident beam into the Stokes vector of the scattered beam, with the scattering plane defined as the plane of the reference of the Stokes parameters. For spherical symmetry, the scattering matrix will be of the relative simple form (Hulst, 1981; Hovenier & van der Mee, 1983, 1988):

$$\mathbf{F}(\Theta) = \begin{bmatrix} a_1(\Theta) & b_1(\Theta) & 0 & 0 \\ b_1(\Theta) & a_2(\Theta) & 0 & 0 \\ 0 & 0 & a_3(\Theta) & b_2(\Theta) \\ 0 & 0 & -b_2(\Theta) & a_4(\Theta), \end{bmatrix} \tag{1.11}$$

where the matrix contains six real functions that depend on the scattering angle. Note that this form of the scattering matrix is valid in the case of (i) Rayleigh scattering with(out) depolarisation effects, (ii) scattering on randomly oriented particles, of which each has a plane of symmetry, and (iii) scattering on an equal number of particles and their mirror particles, both having a random orientation. The first element, $a_1(\Theta)$, is known as the scattering function or *phase function*. $a_1(\Theta)$ is the only element required to calculate scattering when polarisation is ignored, thus may be considered as the probability of scattering of unpolarised light in any given direction. This probability depends on the particle size and shape distribution of the particles, the complex refractive index, and the wavelength of the incident light. $\mathbf{F}(\Theta)$ is often normalized such that, $a_1(\Theta)$, averaged over all scattering directions (Θ, φ) equals 1 (Hansen & Travis, 1974).

Phase matrix

To describe multiple scattering of polarised light in a medium, one needs a function that can describe the direction of the incident and scattered with respect to various scattering planes. The scattering matrix $\mathbf{F}(\Theta)$ for randomly oriented particles is defined with respect to one specific scattering plane, OP_1P_2 see Fig. 1.2. To transform the planes of reference for the incident and scattered light to another scattering plane, $\mathbf{F}(\Theta)$ is multiplied by the rotation matrix (similar to Eq. 1.10). This results in the so-called phase matrix.

While Sobolev (1963) laid important groundwork for understanding scattering and polarisation in radiative transfer, it was Hansen & Travis (1974) who formally introduced the phase matrix as it is widely used in modern radiative transfer and scattering physics. They systematically formulated the phase matrix specifically for scattering processes across arbitrary scattering planes, in a manner that became the standard in atmospheric and planetary sciences. Thereafter, Hovenier & van der Mee (1983) established fundamental relationships relevant to multiple scattering theories and general transfer of polarised light in a plane-parallel atmosphere.

The phase matrix $\mathbf{P}(\Theta)$ for isotropic Rayleigh scattering[2] is given by:

[2]Isotropic Rayleigh scattering yields symmetric, spherical particles that are much smaller than the wavelength of the incident light, e.g. gas molecules. Most real molecules exhibit some level of anisotropy. We refer to Hansen & Travis (1974) for the phase matrix for anisotropic Rayleigh particles in random orientation.

$$\mathbf{P}(\Theta) = \frac{3}{4}\begin{pmatrix} 1+\cos^2\Theta & -\sin^2\Theta & 0 & 0 \\ -\sin^2\Theta & 1+\cos^2\Theta & 0 & 0 \\ 0 & 0 & 2\cos\Theta & 0 \\ 0 & 0 & 0 & 2\cos\Theta \end{pmatrix}, \tag{1.12}$$

The first element, $P_{11} = \frac{3}{4}(1+\cos^2\Theta)$ describes the angular distribution of the scattered intensity, indicating that most light is scattered in directions close to the forward or backward direction, $P_{12} = P_{21} = -\frac{3}{4}\sin^2\Theta$ describes the polarisation change upon scattering, showing that the scattered light can become partially polarised, and $P_{33} = P_{44} = \frac{3}{2}\cos\Theta$ relates to the circular and linear polarisation components and shows how these change as function of scattering angle.

As discussed in this section, the scattering matrix and the phase matrix are fundamentally linked. The phase matrix typically represents a normalized version of the scattering matrix that accounts for various orientations of scattering planes. This enables the phase matrix to describe the angular distribution of scattered light, making it especially valuable in applications such as radiative transfer modelling in planetary atmospheres (e.g. Hansen, 1971; Stam et al., 1999; Karalidi et al., 2013), biomedical optics (Rogers et al., 2014; Kienle et al., 2001), and remote sensing (Myneni et al., 1995; Verhoef, 1998).

1.5 Sources of polarisation

Broad–band polarised light can be created by reflection, refraction, scattering and differential absorption. Light becomes polarised when transmitted through or reflected off surfaces. In the case of optical elements, polarisation optics rely on anisotropic effects, meaning that anisotropy influences the transmission, absorption, or phase delay experienced by different components of the electric field. The way in which light is affected depends on the orientation of its electric field vector relative to the optical axis of the anisotropic medium. A polariser selectively absorbs one of two orthogonal components of the electric field, effectively transmitting only the component aligned with its transmission axis. A wave plate (or retarder) alters the relative phase between two orthogonal electric field components, thereby modifying the overall polarisation. A birefringent crystal spatially separates an incident beam into two beams with orthogonal polarisations and different propagation directions (ordinary and extraordinary rays). Unfortunately, there are also general non-polarimetric optics that unwillingly change the polarisation state of the light.

Polarisation obviously does not only exist in an optical lab environment. There are some sources of polarisation in nature as well. Here we give a short summary of how reflection, refraction, scattering and differential absorption mechanisms produce polarised light in nature.

1.5.1 Surface reflection

Light reflected off dielectric surfaces such as wet surfaces, leaves, or other non-shiny objects will generally become polarised. To which extent depends on the angle of incidence

and the material of the surface. Reflection between two types of media with different refractive indices (e.g. air and glass) can be described using the Fresnel equations (Fresnel, 1819). Surfaces tend to reflect light anisotropically. A bidirectional reflectance distribution function (BRDF; Nicodemus, 1965) defines how light with an incident direction (θ_0, ϕ_0) is reflected off an opaque surface into an outgoing direction (θ, ϕ), where θ is the zenith and ϕ the azimuth angle. The BRDF provides a complete description of the angular distribution of reflected light, which is important for accurately modelling both the intensity and polarisation of radiation when performing radiative transfer simulations.

A Lambertian reflector is a simplified version of the BRDF in which the surface reflects the light in the same way in all directions. This simplification is often adopted in radiative transfer models to reduce the size of look-up tables and speed up calculations, because it avoids storing the full angle-resolved BRDF for every surface and illumination geometry. Although it ignores directional and polarisation-dependent effects, it allows the radiative transfer solver, which already accounts for multiple scattering through the phase matrix, to run efficiently for planetary-scale simulations. The disadvantage of using a Lambertian surface is that it is fully depolarising the incident light and causes systematic angle-dependent biases in derived surface reflectance reducing the anisotropy of reflectance, which might lead to minor errors in reflectance calculations (e.g. Qin et al., 2001; Lyapustin et al., 2010; O'Dell et al., 2012). However, research has shown that for modelling a partially cloudy, Earth-like planet covered in vegetation, the Lambertian surface appears to be a reasonable assumption (Wolstencroft & Breon, 2005; Wolstencroft et al., 2005; Stam, 2008).

There are BRDF models that include polarisation information. Empirical BRDF models for Earth surfaces (e.g. Nadal & Breon, 1999; Maignan et al., 2009) have been created using space-based polarisation measurements[3]. These models can be directly incorporated into radiative transfer calculations, where the phase matrix describes scattering in the atmosphere and the surface reflection contributes an additional polarisation signal at the bottom boundary, improving the accuracy of simulated polarimetric observations.

For every transparent dielectric surface, there is a specific angle of incidence at which light with an electric field polarised parallel to the plane of incidence is perfectly transmitted through with no reflection. This angle is better known as the Brewster angle (Brewster, 1815) . Electric fields orthogonal to the parallel polarisation are reflected, creating a beam of light that is polarised perpendicular to the plane of incidence. This is why this angle is often referred to as the *polarising angle*.

One striking example of a polarised surface reflection is an ocean glint (e.g. McCullough, 2006; Lynch et al., 2011; Shaw & Vollmer, 2017; Trees & Stam, 2022). Oceans are typically dark at most wavelengths due to the absorption of sunlight. However, under certain angles, reflection produces a glint which yields a clear polarimetric signature of liquid water. Solid surfaces, such as ice, sand or any type of vegetation, reflect and scatter light differently. Surfaces that are covered in ice scatter light in a way that produces a weaker polarisation signal compared to liquid water. This difference can be used to distinguish planetary or satellite surfaces that are covered in water from planets covered in ice.

[3]The POLDER, (Deschamps et al., 1994) and PARASOL (Tanré et al., 2011) instrument were the first to provide spectral, directional and polarisation measurements of radiation reflected from the Earth's surface and its atmosphere.

1.5.2 Atmospheric refraction and scattering

Sunlight becomes polarised through scattering by molecules and aerosols in the atmosphere. How a particle scatters the light depends mainly on its size. In the general case of a spherically symmetric particle, its size is expressed through a dimensionless size parameter x, defined by $x = 2\pi r/\lambda$. Here, r is the particle's radius and λ the wavelength of the scattered light. Rayleigh scattering is the elastic scattering of light by tiny particles ($x \ll 1$, e.g. molecules) much smaller than the wavelength of the light. Particles with sizes in the order of the wavelength ($x \approx 1$, e.g. cloud droplets) scatter according to Mie scattering. Geometrical scattering applies to even larger particles ($x \gg 1$, e.g. ice crystals, hail, graupel, rain droplets). These are treated as geometric shapes when determining their scattering properties.

Atmospheric refraction effects are wavelength dependent. A rainbow is a classic example of an atmospheric polarisation phenomenon resulting from white light undergoing two refractions and one internal reflection within water droplets. Due to dispersion, blue light emerges at a smaller angle relative to the incident white light than red light; consequently, blue appears on the inner edge of the rainbow arc and red on the outer edge. This bright arc is known as the primary rainbow. A less commonly observed feature, the secondary rainbow, arises from light that is internally reflected twice within the water droplet. This second reflection not only reduces the intensity but also reverses the colour order. In both primary and secondary rainbows, the internal reflection occurs at angles close to Brewster's angle (approximately 53° for air-to-water and 37° for water-to-air interfaces) enhancing the degree of polarisation in the reflected light. Brewster (1812) showed that the reflected rainbow light was almost fully polarised. A primary rainbow can reach a degree of linear polarisation of 96% and the secondary rainbow one of 90% (Adam, 2002). In atmospheres of distant planets, the occurrence of a rainbow in reflected light is an indicator of spherically shaped atmospheric particles (e.g. Hansen & Travis, 1974; Liou & Takano, 2002; Bailey, 2007; Karalidi et al., 2013).

Polarisation signatures can reveal details about the optical depth, phase, and composition of clouds, (e.g. Karalidi et al., 2012). These atmospheric phenomena provide critical clues to the composition and structure of distant planetary atmospheres, which are essential for assessing their habitability.

1.5.3 Differential absorption

Different polarisation states of light can be absorbed to different degrees by various crystals lattices and chiral molecules. This cam be described by the Mueller matrix in Eq. 1.8. Linear dichroism, m_{12} and m_{13}, occurs when the absorption of light polarised parallel to an orientation axis is larger or smaller than light polarised perpendicular to the axis. Circular dichroism, m_{14}, is the differential absorbance of left- and right-handed circularly polarised light.

Special polymers, like Polaroid, absorb a specific polarisation state while transmitting the rest. As of this property, the polymer can be used as dichroic polarisers. There are also chiral molecules that selectively absorb polarisation states of light. In this work, we focus on a specific group of chiral molecules that occur in only single-handed forms in nature, also known as homochirality (e.g. Guijarro & Yus, 2008; Carroll, 2009; Caglioti et al., 2010). All the basic building blocks of life, like chlorophyll (e.g. Jacobs et al., 1957; Patty et al.,

2017), proteins (Bulheller et al., 2007), amino acids (Amdursky & Stevens, 2015), and sugars (Johnson, 1987), almost exclusively occur in only one enantiomeric form. The exact origin of homochirality remains unknown, (Fuß, 2008; Weller, 2024). Nevertheless, homochirality is an exclusive feature of life on Earth and homochiral molecules induce non-zero fractional circular polarisation. This makes homochirality a powerful tool to search for remote extraterrestrial life by means of polarisation (e.g. Patty et al., 2018a, 2019; Glavin et al., 2019; Gleiser, 2022).

Polarisation provides a wealth of information about planetary atmospheres and surfaces that cannot be obtained from intensity measurements alone. By breaking the cylindrical symmetry of light through reflection, scattering, or interaction with biological molecules, polarisation allows us to probe the physical and chemical properties of distant worlds in unprecedented detail. From detecting oceans and clouds to identifying potential biosignatures, polarisation serves as a powerful tool in the search for habitable planets and extraterrestrial life.

1.6 The measurement of polarisation

Polarimeters are optical instruments used to determine the polarisation properties of light beams and samples. In practice, they perform different intensity measurements after spatial or temporal modulation of the polarisation, which will be explained in more details in Section 1.6.3.

The quality of polarisation measurements relies on accurate and precise control and quantification of the polarisation state of light, as described by the Stokes formalism. This includes not only the orientation of the electric field vector but also the degree and type of polarisation. Various optical elements can be used to manipulate or analyse the polarisation state; those listed below were employed in the research presented in this work.

- A linear polariser polarises incident light by transmitting only the component of the electric field that is aligned with its transmission axis and suppressing the component perpendicular to it. The polarisation axis defines the direction of the electric-field oscillations that are allowed to pass.

- Wave plates are optical devices that introduce a phase shift (a retardance) between two orthogonal components of the electric field vector, typically aligned with the fast and slow axes of a birefringent material. This phase difference enables transformation between different polarisation states, e.g. converting linearly polarised light into circular or elliptical polarisation and vice versa. A quarter-wave plate introduces a $\lambda/4$ phase delay, and a half-wave plate introduces a $\lambda/2$ delay, but only at their design wavelength, λ. Since birefringence depends on wavelength, all single-plate retarders are inherently chromatic, meaning their exact retardance deviates from the nominal value as the wavelength shifts. To minimise this variation, achromatic wave plates are constructed by combining multiple birefringent crystals with their optical axes oriented at specific angles. This configuration compensates for the wavelength dependence of

birefringence across a broader spectral range. Nonetheless, even achromatic designs exhibit residual wavelength-dependent deviations from ideal retardance.

- Fresnel rhombs is a prism that act like a broadband wave plate. They provide a quarter- or half-wave retardance, through respectively two or four internal reflections, over a wider range of wavelengths than a birefringent wave plate.
- Circular polarisers are a combination of a quarter-wave plate with a fast axis orientation of 45° with a linear polariser. The retarder transforms incident circular to linear and vice versa, after which the polariser filters the linear, thus originally circular, polarisation state accordingly.
- Polarising beam splitters separate two orthogonal linear polarisation states, enabling simultaneous measurements of multiple components.
- Polarisation gratings separate left-handed from right-handed circular polarisation while simultaneously dispersing the light (Nikolova & Todorov, 1984; Lajunen et al., 2005; Oh & Escuti, 2007).

1.6.1 Classical polarimeter

A classic example of a polarimeter consist of a rotating wave plate and a (fixed) linear polariser (or e.g. a polarising beam splitter). This configuration allows the polarisation state of the incident light to be modulated and analysed through intensity variations measured by a detector. Depending on the type of wave plate, different components of the Stokes vector are modulated at characteristic frequencies:

- A half-wave plate rotates the plane of linear polarisation, therefore modulating $\mathtt{Q}$ and $\mathtt{U}$. The resulting intensity varies at four times the rotation frequency of the half-wave plate.
- A quarter-wave plate modulates all Stokes parameters. The linear and circular components are modulated at distinct frequencies, allowing the recovery of the full-Stokes vector.

The general expression for the detected intensity as a function of the retarder angle ϕ, its retardance δ, and the polariser angle θ is:

$$\begin{aligned} I_{\text{obs}}(\theta,\phi,\delta) =& \frac{1}{2}(\mathtt{I} + (\mathtt{Q}\cos 2\phi + \mathtt{U}\sin 2\phi)\cos 2(\theta-\phi) \\ &+ [(\mathtt{U}\cos 2\phi - \mathtt{Q}\sin 2\phi)\cos\delta + \mathtt{V}\sin\delta]\sin 2(\theta-\phi)) \\ I_{\text{obs}}(\theta=0^\circ,\phi,\delta) =& \frac{1}{2}(\mathtt{I} + \frac{\mathtt{Q}}{2}[(1+\cos\delta) + (1-\cos\delta)\cos 4\phi] \\ &+ \frac{\mathtt{U}}{2}(1-\cos\delta)\sin 4\phi - \mathtt{V}\sin\delta\sin 2\phi), \end{aligned} \tag{1.13}$$

Fixing the linear polarisation angle to 0° simplifies the expression simplifies: it reveals how the resulting intensity is a combination of the Stokes parameters being modulated with different modulation frequencies. We refer to Snik & Keller (2013) for an elaborate description.

This modulation-based method improves signal-to-noise ratios and enables sensitive polarisation measurements. In dual-beam implementations, the fixed polariser is replaced by a polarising beam splitter, and the two orthogonal polarisation channels are measured simultaneously, further reducing systematic effects due to atmospheric or instrumental variability.

1.6.2 Instrumental polarisation & cross-talk

In astronomical polarimetry, measurements are typically taken after the incoming light has passed through the telescope optics, including multiple reflections on mirrors and lenses. These optical elements can alter the polarisation state of the light, introducing what is referred to as instrumental polarisation: the net polarisation effect introduced by the telescope and/or polarimetric instrument.

The performance of a polarimeter is limited by its systematic effects and noise. We characterise the performance by three key concepts as presented by Snik & Keller (2013), accuracy, efficiency, and sensitivity:

- Polarimetric accuracy refers to how closely the measured Stokes parameters represent the true polarisation state of the source. It is primarily limited by systematic effects and the quality of calibration. For many astronomical polarimeters, typical calibration accuracy reaches the level of 10^{-3} in fractional polarisation (Ichimoto et al., 2008).
- Polarimetric efficiency describes how well each Stokes parameter is transmitted through the system, taking into account the propagation of noise f rom the input to the output. It is defined through the Stokes efficiencies, which are derived from the modulation matrix of the polarimeter.
- Polarimetric sensitivity defines the smallest polarisation signal that can be distinguished above the noise floor. It can be improved through optimized modulation schemes and signal processing techniques, such as lock-in detection.

In addition to these, instrumental cross-talk must be accounted for. Cross-talk refers to the mixing of Stokes parameters introduced by the instrument, e.g., a portion of `Q` appearing in the measurements as `U`. We talk about pure cross-talk if P remains constant while the Stokes parameters are misrepresented (Snik & Keller, 2013). In the case of depolarisation, P is reduced and part of the polarised intensity is lost to `I`, the unpolarised Stokes component. A clear understanding of these effects is crucial for accurate polarimetric measurements.

1.6.3 Polarisation modulation

At the core of any polarimeter is a linear polariser or polarising beam-splitter, commonly referred to as the *analyser*. It selects a specific polarisation state and converts it into a measurable intensity signal at the detector. To control which polarisation state is being analysed, a polarimeter typically includes a *polarisation modulator*. This modulator alters the polarisation state of the incoming light in a controlled way, enabling the analyser to extract different components of the polarisation. To improve polarimetric sensitivity, most polarimeters rely on modulation techniques. These are strategies that transform the incoming polarisation state into measurable intensity variations. These modulation schemes fall into two main categories:

Spatial modulation splits the beam into multiple components that are analysed simultaneously. A common implementation is the dual-beam technique, in which a polarising beam splitter separates orthogonal polarisation states into two beams directed to different regions of the detector. This method enables simultaneous measurement of complementary polarisation states, reducing the effects of seeing or time-varying noise. Differential measurements between the two beams yield the desired polarisation signals with improved precision. See Tinbergen, J. (1996) and Bagnulo et al. (2009) for foundational work on dual-beam polarimetry.

Temporal modulation involves modulating the polarisation state over time using rotating elements, such as linear polarisers or wave plates. By synchronizing these modulations with the detector readout, one can sequentially measure intensities corresponding to different polarisation projections. This approach benefits from the ability to use lock-in detection techniques, which boost signal-to-noise by isolating the modulated polarisation signal from background noise or system drifts. High-frequency modulators, such as photo-elastic modulators (PEMs) or ferroelectric liquid crystals (FLCs), dynamically vary their retardance at kHz rates, thereby modulating the incoming polarisation state over time. For example, PEMs achieve this by applying a periodic stress to an optical element, while FLCs electrically switch between discrete retardance states. This enables real-time modulation of polarisation, making them well-suited for high-sensitivity polarimetry. Kemp et al. (1987) demonstrated a sensitivity of $3 \cdot 10^{-7}$ in measuring the linear polarisation of broad-band sunlight using a PEM-based aperture polarimeter modulating above 30 kHz. Similar high-sensitivity techniques have been applied to stellar polarimetry (Hough et al., 2006) and solar spectropolarimetry (Povel et al., 1994), the latter requiring fast detectors capable of kHz-rate demodulation, reaching sensitivity levels of $10^{-5} - 10^{-6}$. Polarimetric sensitivity at the 10^{-5} level can also be reached using slow modulation, but only when combined with spatial modulation in a dual-beam configuration. This technique is especially advantageous in astronomical applications where there is a shortage of photons since it allows for long exposures and avoids the light loss inherent to single-beam systems.

In all cases, the Stokes parameters are reconstructed via demodulation, a process involving linear combinations of intensity measurements taken at different modulation states. This makes polarimetry a fundamentally differential technique and thus susceptible to any effects that break the assumption of identical measurement conditions like time variations in the source, atmospheric fluctuations, or instrument instability.

While modulation increases sensitivity, it does not inherently correct for systematic errors. Therefore, optimization of both modulation strategies (for sensitivity) and calibration routines (for accuracy) is essential. When combined, these can push polarimetric sensitivity, enabling the detection of very weak polarisation signals in challenging observational environments.

Fresnel–Arago laws

Polarisation describes the orientation of the electric field vector in electromagnetic waves. One distinct but related wave phenomena is interference. Interference describes the interac-

tion of waves, where their amplitudes combine to produce regions of enhanced or reduced amplitude. The interference pattern observed for polarised light depends on the relative polarisation states of the interfering waves.

The Fresnel-Arago laws describe the behaviour of polarised light upon interference. In brief:

- Two waves, that are linearly polarised in the same plane, can interfere.
- Two waves, that are linearly polarised in orthogonal planes, cannot interfere.
- Two waves, that are linearly polarised in orthogonal planes, derived from the same natural light source and brought together into the same plane of polarisation, cannot interfere.
- Two waves, that are linearly polarised in orthogonal planes, derived from the same linear polarised wave source and brought together into the same plane of polarisation, can interfere.

These laws are particularly relevant when analysing the propagation of light through polarisation modulation devices. In spatial modulation schemes, such as those employing liquid crystal polarisation modulators, the local polarisation state of the light varies across the beam. As a result, interference effects may arise due to spatially dependent polarisation transformations, especially in near-field (Fresnel) diffraction patterns observed behind the modulator. Understanding which polarisation components can interfere is essential for interpreting the resulting intensity distributions and optimizing polarimetric system performance.

1.7 Spectropolarimeters

Three spectropolarimeters were used during the research presented in this dissertation. This section will provide a brief overview of their optical set-ups, science goals, and relevant literature.

1.7.1 TreePol & FlyPol

TreePol (Patty et al., 2017, 2018a, 2019) is a circular spectropolarimeter developed by the Astronomical Instrumentation group at the Leiden Observatory. It measures the fractional circular polarisation of transmitted or reflected sunlight as a function of wavelength (400-900 nm) after interaction with a sample or surface.

The polarisation states of the incident light are modulated by a ferro-electric liquid crystal, FLC. This is a fast-switching liquid crystal device capable of actively flipping its fast axis orientation between two discrete angles. This contrasts with the solidified (polymerized) liquid-crystal elements used in spatially patterned modulators, as will be discussed in subsection 1.7.2. The FLC in TreePol functions as a half-wave retarder (at $\lambda = 590$ nm) and can switch orientation at rates up to several kHz. It is followed by a polarising beam splitter that separates the light into two beams with orthogonal linear polarisation states. These beams are directed to a dual-beam spectrograph, each feeding an one-dimensional detector.

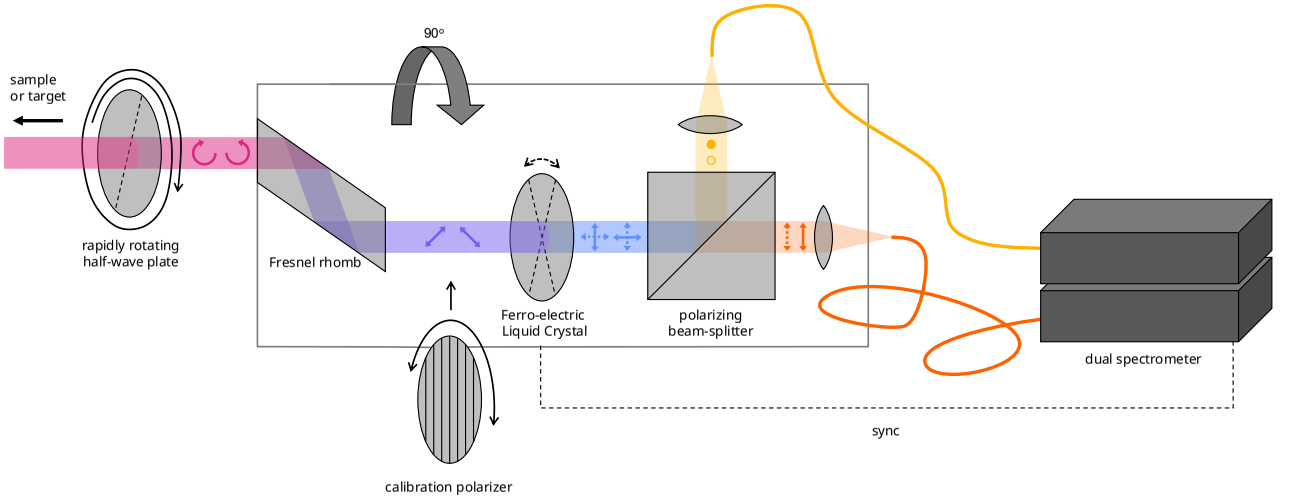

Figure 1.3: Schematic representation of TreePol (after Patty et al. (2017)). A Fresnel rhomb converts circular to linear polarisation (with a rotating half-wave plate before it to reduce instrumental crosstalk). A fast-switching FLC (half-wave at 590 nm) toggles the polarisation between two states, a polarising beam-splitter sends orthogonal states to a dual-beam spectrograph and detectors, and a double-difference demodulation recovers the circular-polarisation spectrum $V(\lambda)$. Treepol's sensitivity is of order 10^{-5}; a calibration polariser can be inserted for calibrations.

TreePol achieves a polarimetric sensitivity of approximately 10^{-5}, which is sufficient to detect the weak circular polarisation signals associated with biological matter. The fast switching of the FLC is synchronized with the high frame rate ($\sim$ 952 fps) of the detectors. However, the sensitivity is ultimately limited by temperature-induced spectral polarisation fringes, which also limit the polarimetric accuracy by masking the true circular polarisation signal.

Figure 1.3 shows the optical set-up of TreePol. After interaction with the sample, a Fresnel rhomb converts the incident circular polarisation into linear polarisation. The FLC continuously toggles its half-wave fast axis orientation between ±22.5°, swapping the polarisation content of the two beams. The polarising beam splitter then separates the beams into horizontal and vertical polarisation states, which are converted into intensity spectra that scale with $[\mathtt{I} \pm \mathtt{V}](\lambda)$, $[\mathtt{I} \mp \mathtt{V}](\lambda)$ respectively. By applying a double-difference scheme (e.g. Clarke & Barocas, 1965; Snik & Keller, 2013; Martí-Vidal et al., 2016), the circular polarisation spectrum $\mathtt{V}\lambda$) is extracted from these redundant intensity spectra. The half-wave plate in front of the Fresnel Rhomb is rapidly and continuously spinning. Doing so, it can mitigate possible linear polarization crosstalk within the instrument.

Using TreePol, Patty et al. (2017) demonstrated in the lab that the antisymmetric circular polarisation signal in the chlorophyll absorption band typical for a leaf in transmission disappears as a leaf dies. This is attributed to the breakdown of the chiral macrostructures formed by chlorophyll molecules as they degrade. Later, Patty et al. (2019) showed the potential of the remote biosignature detection: while healthy vegetation produced clear circular polarisation signals, artificial turf did not.

FlyPol (Patty et al., 2021; Mulder et al., 2022) is an adaptation of the TreePol instrument, constructed in Bern, Switzerland. Its optical configuration is nearly identical, but the Fresnel Rhomb is replaced by an achromatic quarter-wave plate to maintain a straight optical path. The spectrographs were also upgraded for faster, more stable readouts, and active temperature control was added to improve temporal stability. Patty et al. (2021) used FlyPol for the first remote circular polarisation measurements from a helicopter, which was later extended to measurement from a hot-air balloon (Mulder et al., 2022).

1.7.2 Life Signature Detection Polarimeter

The Life Signature Detection Polarimeter (LSDPol; Snik et al., 2019; Keller et al., 2020; Mulder et al., 2021) is a compact, solid-state, snapshot, non-imaging full-Stokes spectropolarimeter designed to remotely detect biosignatures on Earth. Its goal is to conduct circular spectropolarimetric surveys from aerial or orbital platforms, ultimately enabling a mission from a low earth obit, such as using the International Space Station, to globally map the polarisation signature of life on Earth.

The optical design of LSDPol is based on a patterned liquid-crystal polymer with an achromatic quarter-wave retardance and a spatially varying fast-axis orientation. This static polarisation modulator encodes the polarisation state of incoming light into a spatially modulated intensity pattern. The approach of using a spatially varying polymer is derived from the concept of classical polarimetry without moving parts as proposed by Sparks et al. (2019). Their patterned polarisation modulator acts as a quarter-wave plate whose fast-axis angle

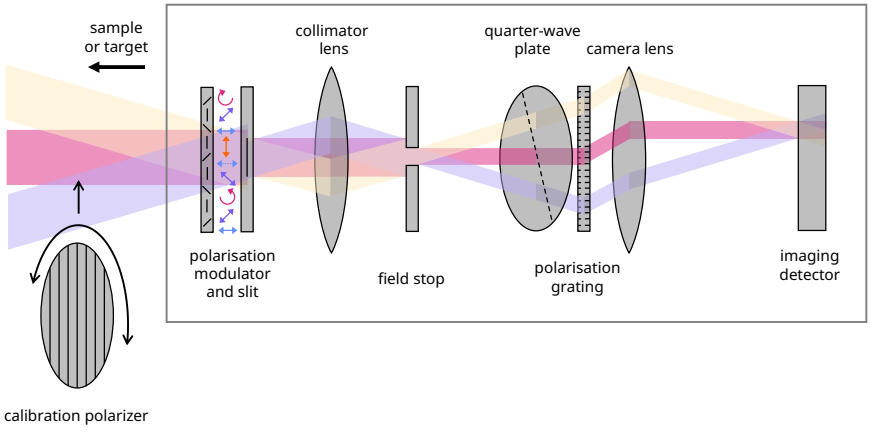

Figure 1.4: Schematic representation of LSDpol. A patterned liquid-crystal quarter-wave plate with a spatially varying fast-axis encodes the incoming Stokes vector as spatial intensity modulations along the slit, so `V`, `Q`, and `U` appear at distinct spatial frequencies. A fixed quarter-wave plate followed by a polarization grating then disperses the light spectrally while separating left- and right-handed circular polarisation into different diffraction orders, allowing full-Stokes retrieval from the modulation at each wavelength.

varies along one spatial direction. This converts circular and linear polarisation into distinct spatial modulation frequencies in the intensity distribution along the slit. Specifically, circular polarisation, `V`, and linear polarisation, `Q` and `U`, manifest as sinusoidal modulations at different spatial frequencies (differing by a factor of two). This spatially modulated light is fed into a long-slit spectrograph, where each wavelength yields a unique intensity modulation profile. Assuming that the polarisation state and illumination are approximately constant along the slit direction, a fit of the theoretical modulation function allows the extraction of full-Stokes parameters. In their concept, Sparks et al. (2019) used a fixed linear polariser as the polarisation analyser. In the LSDpol implementation, the analyser is a fixed quarter-wave plate directly followed by a polarisation grating. The grating acts as both a spectrograph and a circular-polarisation-sensitive beam splitter, separating left- and right-handed circular polarisation into different diffraction orders, while simultaneously dispersing the light spectrally. In theory, this would result in an exceptional snapshot full-Stokes spectropolarimeter.

Despite the sophisticated design, the prototype instrument as described by Keller et al. (2020) suffered from cross-talk between linear and circular polarisation, as well as spurious modulation artifacts in the zeroth diffraction order. The dissertation builds upon this foundation to mitigate these limitations and further develop the technology.

1.8 This dissertation

The overarching aim of this dissertation, **Tracing life through light: Towards detecting life on exoplanets with spectroscopy and spectropolarimetry**, is to explore how light - its spectrum, its polarisation, and the physical processes that transform it - can be used to uncover the nature of distant worlds. The work spans both observational astronomy and instrumental development, reflecting the dual challenge of interpreting atmospheric signatures while designing the tools capable of detecting them[4]. To address this broad goal, the dissertation is structured into two interconnected parts: the first focuses on extracting atmospheric properties from spectroscopic observations of substellar objects, and the second investigates the use of polarisation - both as a biosignature and as a powerful tool in next-generation space-based instrumentation.

Part I: Characterising atmospheres through spectroscopy

Chapter 2: Atmospheric characterization of brown dwarf atmospheres

This part begins by exploring substellar atmospheres as natural laboratories for understanding planetary formation pathways. Brown dwarfs are believed to form through the collapse of molecular clouds (Bate et al., 2002; Whitworth et al., 2007), while giant planets such as super-Jupiters may follow distinct formation pathways involving solid and gas accretion Pollack et al. (1996); Helled et al. (2014). However, atmospheric characteristics of brown dwarfs do resemble those of super-Jupiters in atmospheric characteristics. Despite these different origins, their atmospheric characteristics often show strong similarities, making brown dwarfs particularly valuable for spectroscopic studies as they are significantly more accessible observationally.

We analyse three L-type brown dwarfs, selected from the European Southern Observatory SupJup survey (Program ID: 1110.C-4264, PI: Snellen) (de Regt et al., 2024). Measurements of chemical abundance ratios (C/O) and isotopic ratios (^{12}C/^{13}C) in representative samples of brown dwarfs and super-Jupiters can offer important constraints on formation processes. For the three targets, we retrieved C/O ratios between 0.65 and 0.71, consistent with the solar elemental ratio. The ^{12}C/^{13}C retrievals show strong ^{13}CO signals in two brown dwarfs, and a tentative detection in the third. These ratios appear slightly higher than typical interstellar medium values, suggesting that brown dwarfs may exhibit modestly elevated carbon isotope ratios compared to super-Jupiters.

[4] At least half of the project time was dedicated to simulating and modelling a realistic spectropolarimetric signal of the Earth as it would appear if observed as an exoplanet. These simulations served as an independent validation of the results presented in Gordon et al. (2023), but the associated work is not discussed in this dissertation.

Part II: Observing the Earth as an exoplanet using polarimetry

Chapter 3: Spectropolarimetric measurements of life from a hot-air balloon

Building on the theme of using light as a tracer of life, the second part of this dissertation focuses on the observation of fractional circular polarisation in sunlight reflected from biotic surfaces, such as vegetation. Homochirality is the single handedness of many biomolecules like amino acids, sugars, and photosynthetic pigment–protein complexes, which makes it a fundamental and distinguishing feature of life on Earth. Homochirality is often argued to be widespread among living systems, although its universality beyond Earth remains a hypothesis rather than a certainty. Because homochiral molecules imprint characteristic circular polarisation signatures on reflected light via circular dichroism and supramolecular chiral ordering, measuring this fractional circular polarisation offers a promising remote biosignature (Patty et al., 2019). This makes circular spectropolarimetry a complementary technique to traditional reflectance spectroscopy rather hence a powerful tool to detect life.

To explore how homochiral signals appear under realistic conditions, we used the highly sensitive FlyPol instrument (Patty et al., 2021). This spectropolarimeter measures the fractional circular polarisation, $\mathtt{V/I}$, of incident light within the wavelength range of 400-900 nm, with a sensitivity better $> 10^{-4}$. Observations were carried out from a hot-air balloon, providing an airborne vantage point for measuring vegetation and other Earth surfaces. This platform offers an intermediate step between laboratory measurements and future space-based observations, allowing us to assess how circular polarisation biosignatures evolve with increasing distance and changing illumination geometry while introducing realistic atmospheric and bidirectional reflectance effects.

Observations of diverse scenes - farmland, forests, lakes, and urban areas - allowed us to explore the feasibility of distinguishing biotic from abiotic features. Optimal solar angles and integration times were established that resulted in accurate circular polarisation spectra. We report circular polarisation spectra of grass observed from various heights, measuring $\mathtt{V/I} = 2 \cdot 10^{-3}$ from $\sim$ 20 m and $\mathtt{V/I} = -5 \cdot 10^{-4}$ from $\sim$ 650 m elevation. We did not observe circular polarisation signals from surface water, which is consistent with low concentrations of photosynthetic biomass (e.g. phytoplankton) during early spring and the dominance of reflection suppressing chiral signatures. For subsequent observations of farmland that featured various types of grass, we report a fractional circular polarisation that varies between $\mathtt{V/I} = -9.0 \cdot 10^{-2}$ to 0.25×10^{-2}. The successful detection of circular polarisation from terrestrial vegetation demonstrates that biological activity can imprint measurable polarimetric signatures on reflected light.

Chapter 4: Diffraction effects from spatial polarisation modulators

Building on the demonstration that circular polarisation can be used to remotely probe biological activity on Earth, we now turn to the instrumental requirements for detecting similar signals on exoplanets. Such observations demand sensitivity not only to circular polarisation but to all components of the Stokes vector. This motivates the design of a snapshot full-Stokes spectropolarimeter for space-based observations, LSDpol, whose configuration, challenges,

and diffraction-induced artefacts are examined.

The design of LSDpol incorporates a spatial polarisation modulator in the instruments' entrance slit. This element is implemented as a liquid-crystal quarter-wave retarder with a fast axis that rotates continuously as a function of position along the slit. This spatial modulation allows for simultaneous encoding of polarisation states in a snapshot measurement. Positioned downstream, a second quarter-wave plate together with a polarisation grating serves as both the spectral disperser and the circular-polarisation beam splitter. However, early tests of this configuration revealed significant linear-to-circular cross-talk, complicating the accurate demodulation of the full Stokes parameters.

To identify the origin of this spurious modulation, we carried out numerical simulations exploring several potential sources, including circular-to-linear cross-talk and diffraction effects induced by the structured phase profile of the spatial modulator. Particular attention was given to near-field (Fresnel) diffraction occurring immediately after the modulator, as the rotating fast-axis pattern introduces spatially varying phase delays.

These simulations showed that Fresnel diffraction effects downstream of the spatial polarisation modulator were the dominant contributor to the observed artefacts. Laboratory measurements using fully linearly and circularly polarised input light confirmed these predictions. The findings establish the theoretical and numerical basis for understanding diffraction-induced polarisation artefacts, which is expanded upon in Chapter 5.

Chapter 5: Polarisation-dependent Talbot diffraction in spatial phase modulators

This chapter presents an experimental investigation of diffraction-induced artefacts in full-Stokes spectropolarimetry using Spatial Polarisation Modulators (SPMs). These modulators enable snapshot measurements without moving parts but inherently contain structured phase patterns that can generate polarisation-dependent diffraction effects, most notably the Talbot effect. Such effects introduce unintended intensity modulations that are especially problematic during calibration. Even slight defocusing enhances these modulations, producing patterns that can mimic linear-to-circular polarisation cross-talk and thereby obscure the true polarisation state.

The results highlight the importance of precise optical alignment and rigorous calibration procedures to mitigate these artefacts. A detailed analysis is provided of the polarisation-dependent Talbot effect, supported by visualisations of diffraction arising from phase variations within the modulator. To probe this behaviour further, a linear polarisation analyser was placed after the SPM, and both the input polarisation state and the modulator's retardance were systematically varied. These measurements confirm the strong sensitivity of the system to spatial phase structure and alignment, underscoring the critical role of careful calibration in snapshot full-Stokes spectropolarimetry.